Journal of Alloys and Compounds 526 (2012) 85–90

Contents lists available at SciVerse ScienceDirect

Journal of Alloys and Compounds

journal homepage: www.elsevier.com/locate/jallcom

Structural, dielectric and magnetic properties of Cr–Zn doped strontium hexa-ferrites for high frequency applications

G. Asghar, M. Anis-ur-Rehman*

Applied Thermal Physics Laboratory, Department of Physics, COMSATS Institute of Information Technology, Islamabad 44000, Pakistan

ARTICLE INFO

Article history:
Received 24 April 2011
Received in revised form 8 February 2012
Accepted 13 February 2012
Available online xxx

Keywords:
M-Hexaferrites
Ac conductivity
Dielectric loss
Hysteresis
Dc electrical resistivity

ABSTRACT

M-type strontium hexa-ferrite nano particles with composition $SrFe_{12-2x}Cr_xZn_xO_{19}$ ($X = 0.0, 0.2, 0.4, 0.6, 0.8$) were prepared by co-precipitation method and are reported for the first time. X-ray diffraction analysis confirmed the successful substitution of Cr and Zn ions in the strontium hexa-ferrite lattice. Structural morphology studied by scanning electron micrographs revealed that Cr–Zn doping inhabits the grain growth. Dielectric measurements were taken as a function of frequency in the range (10 kHz to 3 MHz). Both dielectric constants and dielectric losses were found to be decreasing with the increase in Cr–Zn concentration. As Cr–Zn doping favored the decrease in dielectric losses to a large extent (0.32–0.02) so the strontium hexa-ferrite with these dopants is very useful for high frequency applications. The frequency dependent ac conductivity increases sharply at higher frequencies due to increase in hopping frequency of electrons and decrease with the increase in doping concentration and this is due to decrease in Fe^{2+} ions. Temperature dependent dc electrical resistivity measurements showed a decreasing trend with the increase in Cr–Zn concentration. The *M–H* loop indicated that both coercivity and saturation magnetization were decreased with the increase in doping concentration. The former was decreased due to increase in grain size and later was decreased due to weak and non-magnetic cations distribution on interstitial sites.

1. Introduction

M-type hexa-ferrite (M = Ba, Sr, Pb) crystallizes in a magnetoplumbite structure and are a class of important magnetic materials due to their numerous applications such as microwave devices, high density recording media, magneto-optic media, electric motors, magnetic heads, etc. [1–8]. From the viewpoint of microwave devices, ferrites are used into an alternating magnetic field because of their high electrical resistivity, low eddy current loss and excellent magnetic property in high frequency as compared with metal magnetic materials. M-type hexa-ferrites are more useful, for high frequency (GHz) applications than soft ferrites due to their high magneto crystalline anisotropy which resulted in very low residual losses [9–12]. Several synthesis techniques have been used to prepare and tailor the properties of strontium hexa-ferrite nanoparticles [13–17]. Wet-chemical method, along with low synthesis temperature, provides better control on composition and homogeneity [18]. M-type hexa-ferrites crystallize in a hexagonal structure containing 64 ions per unit cell on 11 different symmetry sites. The 24 iron (Fe) atoms are distributed over five distinct interstitial sites: three octahedral sites (12k, 2a, and $4f_2$), one tetrahedral ($4f_1$) site and one bi-pyramidal site (2b). The electrical and magnetic [19] properties of M-type hexa-ferrites can be tailored by using different dopants on these interstitial sites. Strontium hexa-ferrites are famous for their better magnetic properties, high Curie temperature, high corrosion resistance, high chemical stability, high electrical resistivity, low eddy current losses, low cost production and non-toxicity [14,16,20,21]. These excellent properties make the strontium hexa-ferrite useful for high frequency applications. In the present work, effect of the Cr–Zn substitution on structural, electrical and magnetic properties of strontium hexa-ferrite has been reported.

The aim of the present work is to improve the electrical properties of strontium hexa-ferrites and making the material useful for high frequency applications.

2. Experimental details

M-type $SrFe_{12-2x}Cr_xZn_xO_{19}$ with $X = 0.0, 0.2, 0.4, 0.6, 0.8$ were prepared using co-precipitation method. The salts used in the synthesis of samples were $Sr(NO_3)_2$, $Fe(NO_3)_3{\cdot}9H_2O$, $Cr(NO_3)_3{\cdot}9H_2O$, $Zn(NO_3)_2{\cdot}6H_2O$. These salts were dissolved in deionized water and mixed. The mixed solution was heated on a hot plate along with continuous stirring. The calculated volume of the aqueous solution of NaOH was added to get pH of the solution equal to 13 at 70 °C. The final mixed solution was

---

* Corresponding author. Tel.: +92 321 5163059.
E-mail addresses: rehmananis@hotmail.com, marehman@comsats.edu.pk (M. Anis-ur-Rehman).

0925-8388/$ – see front matter © 2012 Elsevier B.V. All rights reserved.
doi:10.1016/j.jallcom.2012.02.086

stirred for 1 h to get fine homogeneity. The precipitates obtained were washed well with de-ionized water and then dried in an oven at 105 °C. The dried powder was sintered in a box furnace for 1 h at 940 ± 5 °C. This sintered powder was converted into pellets by using a uni-axial press. These pellets were sintered at 910 ± 5 °C for 15 min and were used for different characterizations.

3. Results and discussion

3.1. Structural properties

The crystallographic structure and phase formation of the composition $SrFe_{12-2x}Cr_xZn_xO_{19}$ with $X = 0.0, 0.2, 0.4, 0.6, 0.8$ was studied at the room temperature by using powder X-ray diffraction data collected in the step of 0.02° in the 2θ range 25–80° on a PANalytical X-ray diffractometer using CuK_α ($\lambda = 1.5406$ Å) rays. All the peaks of XRD patterns shown in Fig. 1 were identified by using ICDD patterns with reference code 01-080-1197. The indexed XRD patterns show that most of the compositions have a single phase of strontium hexa-ferrite material but in some compositions, the peaks of the secondary phase of α-Fe_2O_3 are detected. All the XRD patterns confirmed the successful substitution of Cr–Zn cations on the interstitial sites of strontium hexa-ferrite lattice as there is no separate peak of these substituted cations is detected. Parameters calculated

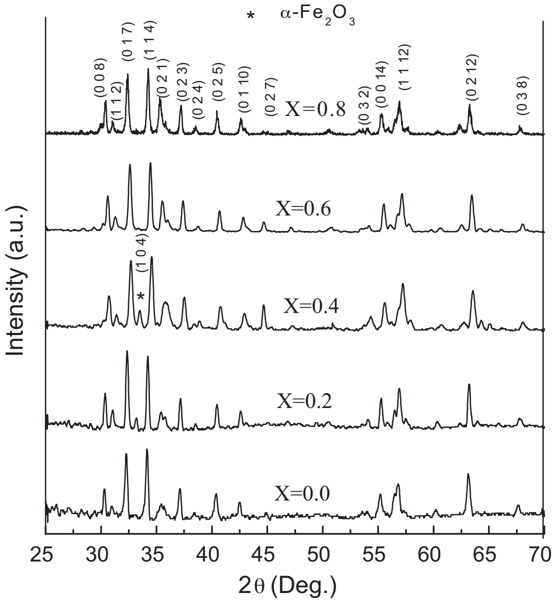

Fig. 1. Indexed XRD patterns of $SrFe_{12-2x}Cr_xZn_xO_{19}$ with $X = 0.0, 0.2, 0.4, 0.6, 0.8$.

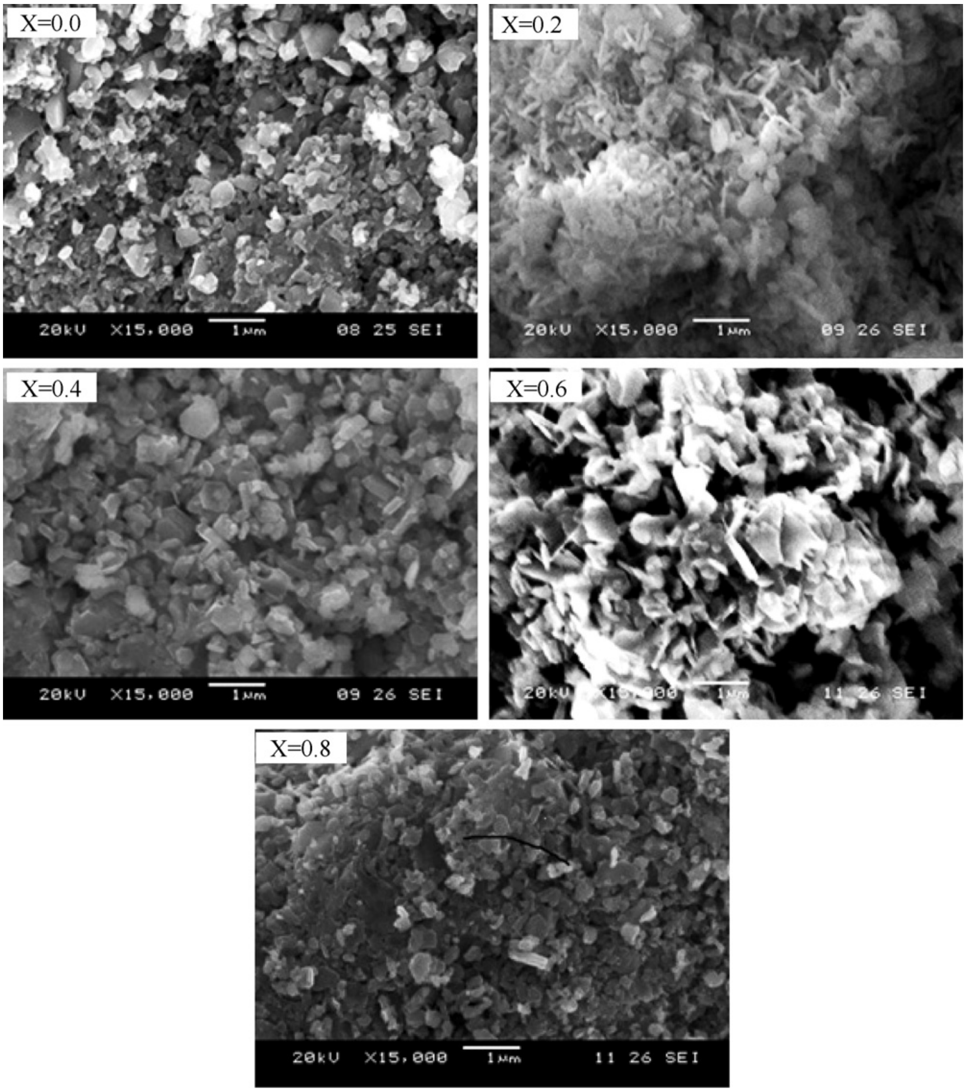

Fig. 2. SEM micrographs of $SrFe_{12-2x}Cr_xZn_xO_{19}$ with $X = 0.0, 0.2, 0.4, 0.6, 0.8$.

Table 1
Lattice parameters (a, c), average crystallite size (D_{av}), X-ray density (ρ_x), activation energy, dc electrical resistivity (ρ_{dc}), dielectric constant (ε'), dielectric loss tangent ($\tan\delta$) and ac conductivity (σ_{ac}) of the prepared samples of $SrFe_{12-2x}Cr_xZn_xO_{19}$ with $X = 0.0, 0.2, 0.4, 0.6, 0.8$.

$SrFe_{12-2x}Cr_xZn_xO_{19}$	0.0	0.2	0.4	0.6	0.8
Lattice constant					
a (Å)	5.884 (2)	5.882 (8)	5.884 (3)	5.884 (2)	5.883 (9)
c (Å)	23.040 (4)	23.028 (2)	23.028 (8)	23.037 (9)	23.036 (9)
Average crystallite size (D_{av})	44	48	30	42	32
X-ray density ρ_x (g/cm^3)	5.10	5.11	5.11	5.11	5.11
Activation energy (eV)	0.94(1)	0.84(1)	0.76(1)	0.67(1)	0.64(1)
Dc resistivity ρ_{dc} (Ω cm) at 200 °C	1.78×10^8	3.08×10^7	1.75×10^7	5.5×10^6	3.65×10^6
Dielectric constant (ε') at 3 MHz	23.04	18.89	16.49	11.09	8.57
Dielectric loss ($\tan\delta$) at 3 MHz	0.32	0.20	0.15	0.08	0.02
Ac conductivity σ_{ac} (S m^{-1}) at 3 MHz	1.25×10^{-3}	6.32×10^{-4}	4.14×10^{-4}	1.48×10^{-4}	2.44×10^{-5}

from indexed XRD patterns are given in Table 1. Crystallite size (D) was calculated by using Scherrer's formula [22] given in Eq. (1).

$$D = \frac{k\lambda}{\beta\cos\theta} \tag{1}$$

where λ is the X-ray wavelength, β is the full width at half maximum, θ is the Bragg angle, and $k = 0.89$.

The crystallite size was in the range 30–48 nm and that is much smaller than already reported [23]. This may be due to the difference in the molarities of the solution.

X-ray density [24] was calculated by using the formula given in Eq. (2).

$$\rho_x = \frac{\text{Number of formula units/unit cell} \times M_m}{V \times N_A} \tag{2}$$

where M_m is molecular mass, V is the volume of unit cell, N_A is Avogadro's number.

Structural morphology was studied by using scanning electron microscopy. The SEM micrographs (Fig. 2) showed that most of the particles are of hexagonal shape and their size has an increasing trend with the increase in Cr–Zn concentration. The average particle size for all compositions was estimated by using the diagonal method and is given in Fig. 3.

3.2. Electrical properties

M-type hexa-ferrites belongs to $P6_3/mmc$ space group and its structure is discussed elsewhere [25,26]. The chemical formula of strontium hexaferrite is $SrFe_{12}O_{19}$. Ideally, this formula contains one divalent cation Sr^{2+}, twelve trivalent cations Fe^{3+} and nineteen divalent anions O^{2-}. Hexa-ferrites synthesized by any method require post synthesis heat treatment at elevated temperatures for phase purity. During heat treatment, some oxygen ions are expected to loss and the resultant chemical formula transforms to $SrFe_{12}O_{19-d}$ form (with d unknown). When one oxygen ion is removed, for charge neutrality, Fe^{3+} ions are transformed to Fe^{2+} ions. During cooling, Fe^{2+} ions in the grain cannot be oxidized and does not change to Fe^{3+}. Electronic transfer between Fe^{3+} and Fe^{2+} is the main electric conduction mechanism of ferrites [27,28]. So the presence of Fe^{2+} ions in hexa-ferrites is the source of charge carriers and is responsible for the conduction mechanism in ferrites. The distance between two metal ions at octahedral (B) site is smaller than the distance between a metal ion at the (B) site and another metal ion at the tetrahedral (A) site. The electron hopping between the (A)–(B) sites under normal conditions, has a very small probability compared with that for (B)–(B) sites hopping. Hopping between (A)–(A) sites, does not exist due to the reason that there are only Fe^{3+} ions at (A) site and any Fe^{2+} ions formed during processing preferentially occupy (B) sites only. In ferrites, the conduction is because of the electron hopping from Fe^{2+} and Fe^{3+} ion present at the octahedral (B) sites [27–29]. The presence of this Fe^{2+} also contributes a lot to the dielectric properties of ferrites. It is reported in the literature that Cr^{3+} ions preferentially occupy the octahedral (B) sites [30] where it replaces Fe^{3+} ions while Zn^{2+} ions occupy the tetrahedral (A) and bipyramidal (C) sites [31] where it replaces Fe^{3+}. In hexaferrites, it is reported that when a cation is replaced with another cation having different valence states then for the charge neutrality this difference is compensated by Fe ions ($Fe^{2+} \leftrightarrow Fe^{3+}$) [5,32,33]. When Zn^{2+} ion replaces Fe^{3+} ion, for charge neutrality, the Fe^{2+} ions present on octahedral B site [34,35] are converted into Fe^{3+} ions. The hopping probability depends upon the separation between the ions involved and activation energy [36].

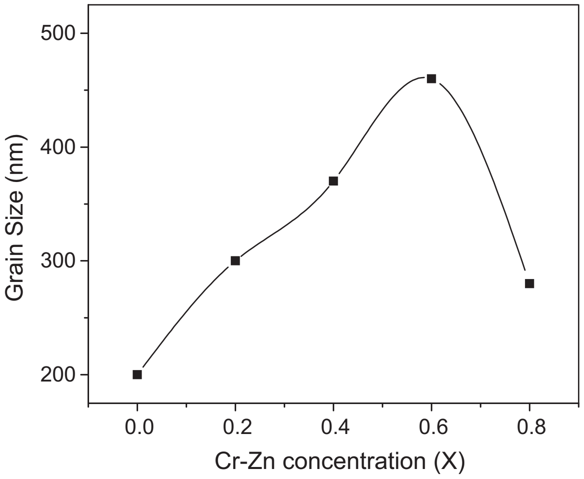

Fig. 3. Plot of grain size (nm) as a function of Cr–Zn concentration for $SrFe_{12-2x}Cr_xZn_xO_{19}$ with $X = 0.0, 0.2, 0.4, 0.6, 0.8$.

3.2.1. Dielectric properties

Different models [37] have been used to explain the dielectric properties of materials. For solids, Maxwell–Wagner two-layer model [38,39] is being commonly used. According to Maxwell–Wagner two layer model for the bulk materials, the grain acts as a resistor and the grain boundary acts as a thin insulating layer [40]. The dielectric properties are measured at room temperature in the frequency range (10 kHz to 3 MHz) using precision component analyzer.

The graph shown in Fig. 4 reveals that the dielectric constants ε' for all compositions decrease sharply at lower frequencies and then becomes fairly constant for higher frequencies. According to Iwauchi [41], the dielectric polarization mechanism in ferrites is similar to their conduction mechanism (due to hopping of electrons between ions of the same element present in more than one valence state). At low frequency, hopping of the electrons could easily follow the applied field and results in the large polarization and hence large dielectric constant.

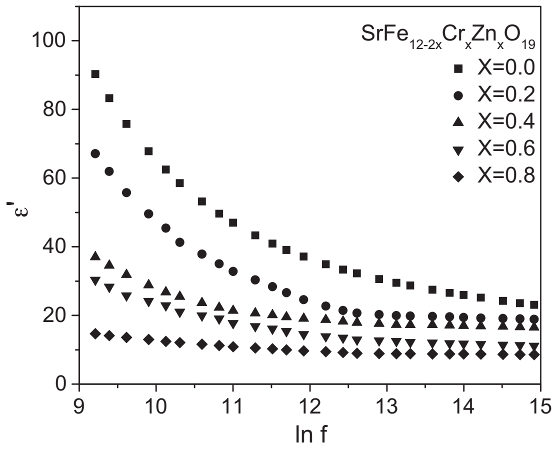

Fig. 4. Plot of dielectric constant (ε') as a function of ln of frequency for $SrFe_{12-2x}Cr_xZn_xO_{19}$ with $X = 0.0, 0.2, 0.4, 0.6, 0.8$.

At high frequency, the hopping of the charge could not follow the applied field and the only local charge polarization could take place and hence net dielectric constant decreases. The graph also indicates that ε' have a decreasing trend with the increase in doping contents. This is due to the fact that in ferrites, the space charge polarization directly depends upon Fe^{2+} ion concentration in a grain. As Zn^{2+} ions have strong preference to occupy tetrahedral (A) sites, so concentration of Fe^{2+} ions on tetrahedral site decreases. So electric polarization decreases and consequently the dielectric constant ε' also decreases. This may also be due to the reason that the Cr ions do not participate in the conduction process but impedes the motion of charge carriers [42,43].

The general trend of the dielectric loss tangent (tan δ) as a function of frequency is shown in Fig. 5. The cause of dispersion at lower frequency is the same as that for dielectric constant. Fig. 5 also shows that the dielectric loss tangent also decreases with the increase in doping concentration. This may be due to the decrease in Fe^{2+} ion concentration, which is responsible for conduction losses, because of the increase in Zn^{2+} content as explained earlier. Values of the dielectric loss tangent obtained from this composition of strontium hexa-ferrite are much smaller than reported in [44,45] so making this substitution ($X = 0.2–0.8$) more suitable for high frequency applications.

The plot of the dielectric loss factor (ε'') shown in Fig. 6 indicates that it decreases initially with the increase in frequency and then becomes fairly constant at higher frequencies. It is because hopping of the electrons could not follow the applied frequency and consequently the dielectric loss factor (ε'') decreases. The decrease in dielectric loss factor (ε'') with the increase in Cr–Zn doping is due to the decrease in Fe^{2+} ion concentration.

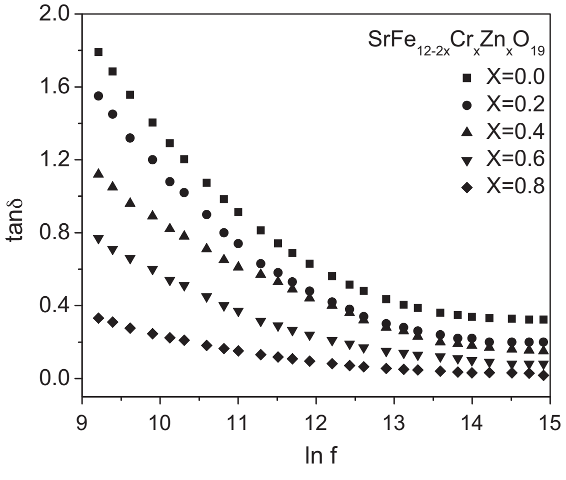

Fig. 5. Plot of dielectric loss (tan δ) as a function of ln of frequency for $SrFe_{12-2x}Cr_xZn_xO_{19}$ with $X = 0.0, 0.2, 0.4, 0.6, 0.8$.

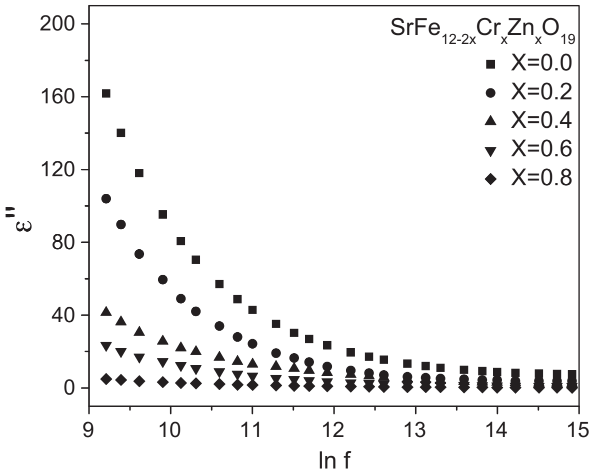

Fig. 6. Plot of dielectric loss factor (ε'') as a function of ln of frequency for $SrFe_{12-2x}Cr_xZn_xO_{19}$ with $X = 0.0, 0.2, 0.4, 0.6, 0.8$.

3.2.2. Room temperature ac conductivity

The ac conductivity (σ_{ac}) is calculated by using formula:

$$\sigma_{ac} = \omega \varepsilon_0 \varepsilon' \tan \delta \tag{3}$$

where $\omega = 2\pi f$.

Fig. 7 shows that σ_{ac} increases up to the relaxation frequency and then decreases and becomes constant for a range of frequencies and then starts increasing at higher frequencies. The hopping frequency of the electrons is smaller at lower frequencies and it increases with the increase in frequency. This is attributed to the fact that the required energy correlated with forward–backward hopping is only a fraction of the energy necessary to activate long range diffusive conduction [46].

3.2.3. Temperature dependent dc electrical properties

The temperature dependent dc electrical resistivity was measured in the range of 373–623 K. Plot of ln of dc electrical resistivity as a function of $1/k_BT$ is shown in Fig. 8. The dc electrical resistivity decreases with the increase in the temperature due to increase

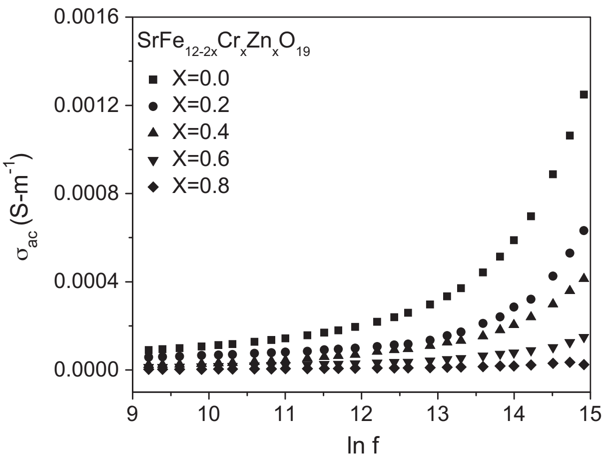

Fig. 7. Plot of ac conductivity as a function of ln of frequency for $SrFe_{12-2x}Cr_xZn_xO_{19}$ with $X = 0.0, 0.2, 0.4, 0.6, 0.8$.

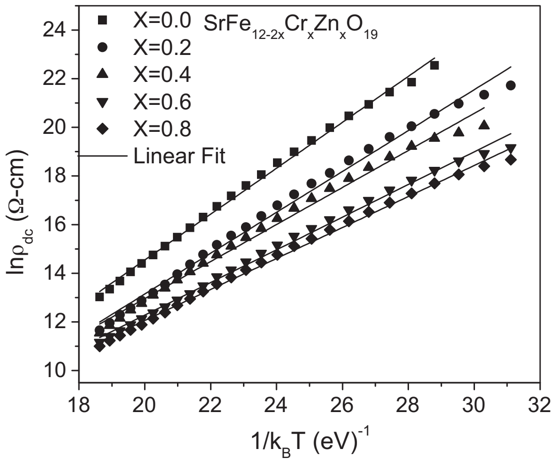

Fig. 8. Plot of ln ρ as a function of $1/k_BT$ for $SrFe_{12-2x}Cr_xZn_xO_{19}$ with $X = 0.0, 0.2, 0.4, 0.6, 0.8$. Line shows the linear fit, the slope of that was used to calculate the activation energy.

in drift mobility of charge carriers. The plot also indicates that resistivity has a decreasing trend with the increase in Cr–Zn concentration. This is because of the increase in the grain size. As the grain size increases, grain boundaries (which acts as highly resistive medium) decreases and consequently resistivity decreases. The effect of grain boundaries has suppressed the effect of decrease in carrier concentration due to decrease in Fe^{2+} ions. Activation energy was calculated from the slope of the linear plots of ln ρ versus reciprocal of the temperature using Arrhenius relation [47] shown in Fig. 8.

Arrhenius relation is given by

$$\rho = \rho_o \exp\left(\frac{E_a}{k_BT}\right) \tag{4}$$

where ρ is resistivity at temperature T, ρ_o is resistivity at $1/T = 0$, E_a is the activation energy and k_B is Boltzmann's constant.

Values of the activation energy as given in Table 1, also decrease with the increase in doping content and that is due to increase in grain the size.

4. Magnetic properties

The magnetic parameters such as coercivity (H_c), saturation magnetization (M_s) and remanence (M_r) are calculated from hysteresis loops of the composition $SrFe_{12-2x}Cr_xZn_xO_{19}$ with $X = 0.0, 0.2, 0.4, 0.6, 0.8$ and are shown in Fig. 9.

The particles formed in all composition are a single domain, as the critical size for single domain grain in case of strontium hexaferrite is 650 nm [48] which is greater than the size of the grains observed. The saturation magnetization (M_s) also decreases with the increase in Cr–Zn concentration. It is due to the substitution of Cr–Zn cations on different interstitial sites. In M-type hexa-ferrite, 24 Fe^{3+} ions are distributed on five different interstitial sites. There are three octahedral (2a, 12k and 4f2), one tetrahedral (4f1), and one trigonal bipyramidal (2b) site. The sites (2a, 12k and 2b) are parallel and (4f1 and 4f2) are antiparallel. The iron atoms present on these sites are coupled by superexchange interactions through the O^{2-} ions, form the ferrimagnetic structure [49–51]. The M-type hexaferrite (magnetoplumbite structure) contains two formula units per unit cell. 12 Fe^{3+} ions are arranged with eight spins in the up direction and four in the down direction, giving a net moment of 4 Fe^{3+} ions per formula unit times 5 μ_B per ion, which gives a total of 20 μ_B per formula unit [52].

According to ferrimagnetic theory [53], magnetism in ferrite originates from the net magnetic moment of ions with spin up and spin down in interstitial sites. Fig. 10 indicates that saturation magnetization decreases with the increase in doping content. The saturation magnetization mainly depends upon the distribution of Cr^{3+} ions on interstitial sites and then magnetic dilution with the substitution of Fe^{3+} ions by the lower magnetic moment ions. It is reported that Cr^{3+} ions with the magnetic moment (3 μ_B) preferentially occupy 12k and 2a sites with spin up. This results in a decrease of the total magnetic moment due to cations with spin up. As the net magnetic moment of one formula unit is due to the difference of the magnetic moments of cations with spin up and spin down so net moment decreases and hence saturation magnetization decreases [21]. On the other hand, Zn with zero magnetic moment occupy the tetrahedral (A) site with spin down and bipyramidal (C) site with spin up [31]. If Zn ions only occupy tetrahedral site then saturation magnetization should increase but the results shows that it decreases. It is possible only if the Zn ions also occupy the sites with spin up. The third factor which also

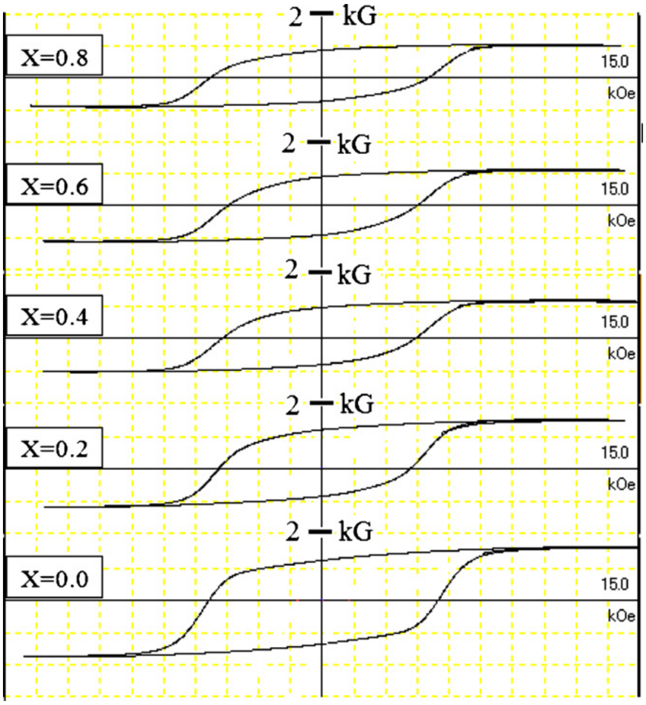

Fig. 9. Hysteresis loops of $SrFe_{12-2x}Cr_xZn_xO_{19}$ ($X = 0.0, 0.2, 0.4, 0.6, 0.8$).

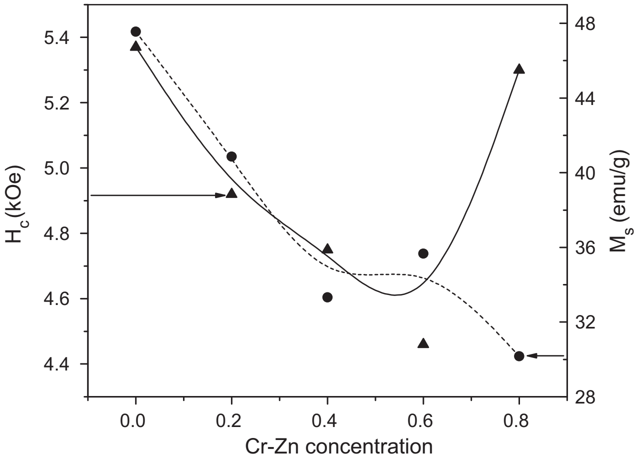

Fig. 10. Plot of coercivity and saturation magnetization versus Cr–Zn concentration of $SrFe_{12-2x}Cr_xZn_xO_{19}$ ($X = 0.0, 0.2, 0.4, 0.6, 0.8$).

contributes to decrease in saturation magnetization is the formation of non magnetic phase (α-Fe_2O_3). The XRD patterns shown in Fig. 1 indicate that the compositions ($X = 0.2$ and 0.4) have non-magnetic phase (α-Fe_2O_3). This non-magnetic phase also contributes to the sharp decrease in saturation magnetization of these compositions. A small increase in saturation magnetization for $X = 0.6$ is due to the absence of this phase. Fig. 10 also shows that coercivity decreases with the increase in Cr–Zn content. This decrease in coercivity (H_c) of the samples ($X \leq 0.6$) is attributed to the increase in grain size (Fig. 3). Decrease in the grain boundaries due to increase in the grain size results in a decrease in opposition to the domain-wall motion and consequently in the coercivity. For $X = 0.8$, it increases due to decrease in particle size.

5. Conclusions

Cr–Zn doped strontium hexa-ferrite ($SrFe_{12-2x}Cr_xZn_xO_{19}$ with $X = 0.0$, 0.2, 0.4, 0.6, 0.8) powder was synthesized by the co-precipitation method. The substitution of Cr and Zn ions in the strontium hexa-ferrite lattice was confirmed by X-ray diffraction analysis. SEM micrographs revealed that Cr–Zn doping causes the increase in grain size. Both dielectric constants and dielectric losses were measured as a function of frequency in the range (10 kHz to 3 MHz). These were decreased with the increase in doping content due to decrease in Fe^{2+} ions. Cr–Zn substitution was proved good for high frequency applications due to decrease in dielectric losses. The ac conductivity was increased sharply at the higher frequency due to increase in hopping frequency of electrons and decreased with the increase in doping concentration due to decrease in Fe^{2+} ions. Temperature dependent dc electrical resistivity measurements showed a decreasing trend with the increase in Cr–Zn concentration due to decrease in grain boundaries. The magnetic measurements obtained from M–H loops indicated that both the coercivity and the saturation magnetization were decreased with the increase in doping concentration. The coercivity was decreased due to increase in grain size and magnetization was decreased due to the substitution of weak and non-magnetic Cr–Zn ions on different interstitial sites.

Acknowledgements

Higher Education Commission of Pakistan is highly acknowledged for providing financial support through “Indigenous 5000 Scholarship Program” and NRPU #893. Dr. M. S. Awan is appreciated for useful assistance.

References

[1] N. Yang, H. Jia, J. Pang, J. Alloys Compd. 438 (2007) 262.
[2] J. Jiang, L.H. Ai, J. Alloys Compd. 502 (2010) 488.
[3] S. Hussain, A. Maqsood, J. Alloys Compd. 466 (2008) 293.
[4] Y.P. Fu, C.H. Lin, K.Y. Pan, J. Alloys Compd. 349 (2003) 228.
[5] C.A. Stergiou, G. Litsardakis, J. Alloys Compd. 509 (2011) 6609.
[6] M.J. Iqbal, R.A. Khan, S. Takeda, S. Mizukami, T. Miyazaki, J. Alloys Compd. 509 (2011) 7618.
[7] M.J. Iqbal, S. Farooq, J. Alloys Compd. 493 (2010) 595.
[8] N. Chen, K. Yang, M. Gu, J. Alloys Compd. 490 (2010) 609.
[9] S. S. Somiya, F. Aldinger, N. Claussen, R.M. Spriggs, K. Uchino, K. Koumoto, M. Kaneno (Eds.), Handbook of Advanced Ceramics, vol. II, Processing and their Applications, Academic Press, Elsevier Inc., London, UK, 2003.
[10] G.M. Rai, M.A. Iqbal, K.T. Kubra, J. Alloys Compd. 495 (2010) 229.
[11] I. Khan, I. Sadiq, M.N. Ashiq, M.-U.-D. Rana, J. Alloys Compd. 509 (2011) 8042.
[12] Z. Pang, X. Zhang, B. Ding, D. Bao, B. Han, J. Alloys Compd. 492 (2010) 691.
[13] M. Jean, V. Nachbaur, J. Bran, J.M. Le Breton, J. Alloys Compd. 496 (2010) 306.
[14] A. Davoodi, B. Hashemi, J. Alloys Compd. 509 (2011) 5893.
[15] M.J. Iqbal, M.N. Ashiq, P. Hernández-Gómezc, J. María Muñoz Muñoz, C.T. Cabrerac, J. Alloys Compd. 500 (2010) 113.
[16] S.V. Ketov, Yu.D. Yagodkin, V.P. Menushenkov, J. Alloys Compd. 509 (2011) 1065.
[17] S.E. Jacobo, C. Herme, P.G. Bercoff, J. Alloys Compd. 495 (2010) 513.
[18] M.M. Rashad, M. Radwan, M.M. Hessien, J. Alloys Compd. 453 (2008) 304.
[19] P. Brahma, A.K. Giri, D. Chakravorty, M. Tiwari, D. Bahadur, J. Magn. Magn. Mater. 102 (1991) 109.
[20] C.L. Yuan, Y.S. Hong, C.H. Lin, J. Magn. Magn. Mater. 323 (2011) 1851.
[21] R.C. O’Handley, Modern Magnetic Materials, John Wiley & Sons Inc., New York, 1999.
[22] M.N. Ashiq, M.J. Iqbal, I.H. Gul, J. Magn. Magn. Mater. 323 (2011) 259.
[23] M.M. Hessien, M.M. Rashad, K. El-Barawy, J. Magn. Magn. Mater. 320 (2008) 336.
[24] M. Anis-ur-Rehman, G. Asghar, J. Alloys Compd. 509 (2011) 435.
[25] J.C. Burfoot, Ferroelectrics: An Introduction to the Physical Principles, D.Van Nostrand, London, 1967.
[26] E.F. Gorter, Proc. IEEE 104B (1957) 255S.
[27] C.M. Fang, F. Kools, R. Metselaar, G. de With, R.A. de Groot, J. Phys.: Condens. Matter 15 (2003) 6229.
[28] Y. Bai, F. Xu, L. Qiao, J. Zhou, J. Alloys Compd. 473 (2009) 505.
[29] D. Seifert, J. Topfer, F. Langenhorst, J.M. Le Breton, H. Chiron, L. Lechevallier, J. Magn. Magn. Mater. 321 (2009) 4045.
[30] S. Ounnunkad, P. Winotai, J. Magn. Magn. Mater. 301 (2006) 292.
[31] A.G. Angeles, G.M. Suarez, A. Gruskova, M. Papańova, J. Slama, Mater. Lett. 59 (2005) 26.
[32] X. Liu, W. Zhong, S. Yang, Z. Yu, B. Gu, Y. Du, Phys. Status Solidi A 193 (2) (2002) 314.
[33] S. Ounnunkad, Solid State Commun. 138 (2006) 472.
[34] M.J. Iqbal, M.N. Ashiq, I.H. Gul, J. Magn. Magn. Mater. 322 (2010) 1720.
[35] M. Pal, P. Brahma, B.R. Chakraborty, D. Chakravorty, J. Appl. Phys. 36 (1997) 2163.
[36] A. Lakshman, P.S.V.S. Rao, B.P. Rao, K.H. Rao, J. Phys. D: Appl. Phys. 38 (2005) 673.
[37] A.K. Jonscher, J. Phys. D: Appl. Phys. 32 (1999) 57.
[38] J.C. Maxwell, A Treatise on Electricity and Magnetism, vol. 1, Oxford University Press, USA, 1998.
[39] K.W. Wagner, Ann. Phys. (Leipzig) 40 (1913) 817.
[40] H. Neuman, G. Arlt, Ferroelectrics 69 (1986) 179.
[41] K. Iwauchi, Jpn. J. Appl. Phys. 10 (1971) 1520.
[42] A.A. Sattar, A.H. Wafik, H.M. El-Sayed, J. Mater. Sci. 36 (2001) 4703.
[43] K.H. Rao, S.B. Raiju, K. Aggarwal, R.G. Mendiratta, J. Appl. Phys. 52 (1981) 1376.
[44] M.N. Ashiq, M.J. Iqbal, I.H. Gul, J. Alloys Compd. 487 (2009) 341.
[45] M.J. Iqbal, M.N. Ashiq, P.H. Gomez, J.M. Munoz, J. Magn. Magn. Mater. 320 (2008) 881.
[46] M.P. Kumar, T. Sankarappa, B.V. Kumar, N. Nagaraja, Solid State Sci. 11 (2009) 214.
[47] T. Abbas, M.U. Isalm, M.A. Chaudhry, Mod. Phys. Lett. B 9 (22) (1995) 1419.
[48] Z.F. Zi, Y.P. Sun, X.B. Zhu, Z.R. Yang, J.M. Dai, W.H. Song, J. Magn. Magn. Mater. 321 (2009) 2378.
[49] L. Lechevallier, J.M. Le Breton, J.F. Wang, I.R. Harris, J. Magn. Magn. Mater. 269 (2004) 192.
[50] M. Pieper, A. Morel, F. Kools, J. Magn. Magn. Mater. 242 (2002) 1408.
[51] A. Morel, J.M. Le Breton, J. Kreisel, G. Wiesinger, F. Kools, P. Tenaud, J. Magn. Magn. Mater. 242 (2002) 1405.
[52] A. Goldman, Modern Ferrite Technology, 2nd ed., Springer, Pittsburgh, PA, 2006.
[53] R.J. Parker, Proceedings of ICF-3, 1980.